

Oxidation-Reduction Molecular Junction Covalent Organic Frameworks for Full Reaction Photosynthesis of H₂O₂

Jia-Nan Chang, Qi Li, Jing-Wen Shi, Mi Zhang, Lei Zhang, Shan Li, Yifa Chen,*
 Shun-Li Li, and Ya-Qian Lan*

Abstract: The full reaction photosynthesis of H₂O₂ that can combine water-oxidation and oxygen-reduction without sacrificial agents is highly demanded to maximize the light-utilization and overcome the complex reaction-process of anthraquinone-oxidation. Here, a kind of oxidation-reduction molecular junction covalent-organic-framework (TTF-BT-COF) has been synthesized through the covalent-coupling of tetrathiafulvalene (photo-oxidation site) and benzothiazole (photo-reduction site), which presents visible-light-adsorption region, effective electron-hole separation-efficiency and photo-redox sites that enables full reaction generation of H₂O₂. Specifically, a record-high yield (TTF-BT-COF, ≈276000 μMh⁻¹g⁻¹) for H₂O₂ photosynthesis without sacrificial agents has been achieved among porous crystalline photocatalysts. This is the first work that can design oxidation-reduction molecular junction COFs for full reaction photosynthesis of H₂O₂, which might extend the scope of COFs in H₂O₂ production.

Introduction

Hydrogen peroxide (H₂O₂) is a versatile oxidant that can be used as environmentally friendly disinfectant to inactivate pathogenic microorganisms or pollutants (e.g., organochlorine pesticides, cyanide, phenols and antibiotics, etc.) and personal care products owing to its mild and environmentally friendly nature.^[1] The global demand of H₂O₂ is growing rapidly, reaching US\$4.0 billion in 2017 and is expected to further increase to around US\$5.5 billion by 2023.^[1b,2] During past years, the production of H₂O₂ has reached 5.5 million ton in 2015 and increased to 6.5 million tons by 2022, yet it still has a huge gap to be filled and requires more green/economic techniques to meet the

demand.^[3] In recent years, H₂O₂ has also been newly explored as potential energy carrier to replace H₂ in single chamber fuel cell due to its theoretical output potential of fuel cell (1.09 V) is equivalent to that of traditional hydrogen fuel cell (H₂) (1.23 V), meanwhile it is more convenient in storage and transportation than H₂.^[4] To date, the methods for producing H₂O₂ mainly include persulfate electrolysis, electrochemical oxygen reduction, isopropanol oxidation, the direct synthesis of hydrogen peroxide from H₂ and O₂, and anthraquinone oxidation.^[5] Persulfate electrolysis is the main method to produce H₂O₂ in the first half of the 20th century, yet the energy consumption is too large and limited to small-scale production. After that, the isopropanol oxidation process has been developed, while it is still obstructed by the by-product (i.e. acetone) and isopropanol consuming, which has been eliminated at present. Both the direct synthesis of hydrogen peroxide and electrochemical oxygen reduction methods have the problem of low efficiency. In contrast, anthraquinone (AQ) oxidation method is the main method for industrial production of H₂O₂ at present and ≈95% of the global amount of H₂O₂ is produced by this method.^[6] However, this method involves drawbacks like: i) the use of large amount of organic solvents (e.g., heavy aromatics and trioctyl phosphate); ii) the generally applied expensive palladium-based catalysts; iii) the degradation of anthraquinone molecules and iv) complex reaction processes (e.g., catalyst hydrogenation and oxidation processes, etc.), and the palladium catalysts commonly used in the traditional AQ oxidation process are easy to polymerize and agglomerate to reduce hydrogenation activity.^[7] Therefore, it is much essential to develop economic, green and highly efficient catalysts or methods to produce H₂O₂.

As a kind of environmental benign catalytic system, the ideal H₂O₂ photosynthesis system only requires abundant water and oxygen on earth as raw materials, and uses sunlight as green energy to activate photocatalyst and drive oxidation-reduction reactions, which can perfectly meet the sustainable development target and get rid of pollution emission by traditional methods.^[8] In general, the full reaction photosynthesis of H₂O₂ includes two possible pathways: oxygen reduction reaction (ORR) and water oxidation reaction (WOR). Previous studies have shown that in order to realize the photosynthesis of H₂O₂ through oxygen reduction reaction (ORR), the photocatalyst needs to have a more negative LUMO than the O₂ reduction potential (H₂O₂/O₂, theoretically 0.68 V vs. NHE) and it seems that most of the reported photocatalysts are easier to meet the

[*] Dr. J.-N. Chang, Q. Li, J.-W. Shi, S. Li

Jiangsu Collaborative Innovation Centre of Biomedical Functional Materials, Jiangsu Key Laboratory of New Power Batteries, School of Chemistry and Materials Science, Nanjing Normal University Nanjing 210023 (P. R. China)

Dr. M. Zhang, L. Zhang, Prof. Y. Chen, Prof. S.-L. Li, Prof. Y.-Q. Lan
 School of Chemistry, South China Normal University
 Guangzhou, 510006 (P. R. China)

E-mail: chyf927821@163.com

yqlan@njnu.edu.cn

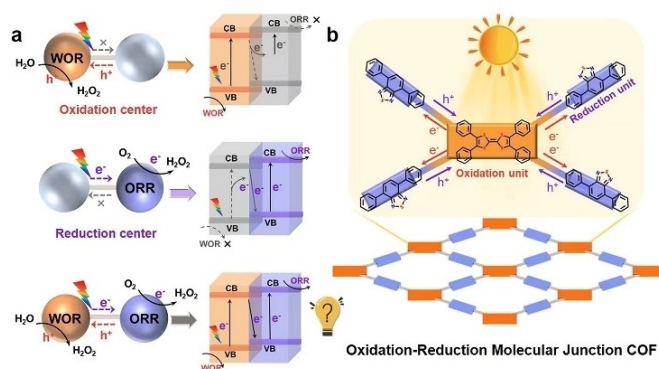
yqlan@m.scnu.edu.cn

requirement of producing H_2O_2 by ORR.^[9] For water oxidation reaction (WOR), there are three competing pathways: including two-electron transfer for H_2O_2 production (1.76 V versus normalized hydrogen electrode, NHE), four-electron transfer for oxygen evolution (1.23 V versus NHE) and one-electron transfer to form hydroxyl radicals (2.38 V versus NHE).^[8b] To achieve the high efficiency in H_2O_2 photosynthesis, the WOR is vital to balance the overall photocatalytic system and it is desirable to boost the 2e^- WOR rather than 4e^- WOR for oxygen evolution, yet it is not easy to achieve due to its uphill thermodynamics (1.76 V versus normalized hydrogen electrode, NHE) and thus some replaced sacrificial agents like methanol oxidation need to be applied.^[10] In this regard, the most efficient and energy-saving way is to realize the full reaction photosynthesis of H_2O_2 , that is, the simultaneous production of H_2O_2 by both WOR and ORR without the use of sacrificial agents, so as to maximize the energy utilization.^[8a,11] To this end, multi-requirements would be needed for the design of photocatalysts, for example, wide light absorption region, appropriate energy band structure, and efficient utilization of photogenerated electrons/holes, apart from the basic need of both photo-reduction and oxidation property. At present, TiO_2 , $\text{g-C}_3\text{N}_4$ and some semiconductors are the most widely used catalysts in the photosynthesis of H_2O_2 , with high chemical/thermal stability, low cost and toxicity, and light corrosion resistance, etc.^[12] However, their applications in the photosynthesis of H_2O_2 still face the following shortcomings: i) the catalysts have wide band gap and requires UV light (<5% of solar radiation) for photo-activation; ii) the band gap of photocatalyst cannot meet the requirements of water oxidation, thus the sacrificial agent needs to be added and iii) most of them lack in developed pores or clear crystal structure, resulting in less exposure of catalytic sites, which is not conducive to transfer mass and the study of catalytic mechanism. Despite some promising photocatalysts like linear conjugated polymers (e.g., poly(3-4-ethynylphenyl)-ethynyl) pyridine (DE7)),^[13] single atom catalyst (such as Sb-SAPC) or molecular catalysts (e.g., ZnPPc-NBCN) have been reported and achieved inspiring results,^[1a,13] most of them still pay less attention to the WOR process and lack in related mechanism research. Therefore, in order to meet the strict requirements of high-efficiency full reaction photosynthesis of H_2O_2 , it is necessary to develop powerful photocatalysts with suitable photo-redox ability to accomplish both WOR and ORR for H_2O_2 production.

Covalent organic frameworks (COFs), composed of light-weight elements and connected by strong covalent bonds, possess well-defined crystal structures, predictable topology, high stability and porosity, etc.^[14] COFs might serve as alternative materials in full reaction photosynthesis of H_2O_2 mostly attributed to the following reasons: i) compared with other materials with higher density, COFs with low density and high porosity might provide more exposed surface area and active sites that can be assessable for the substrates; ii) the tunable structure might endow COFs with efficient ligand-ligand charge transfer (LLCT) effect to realize the effective separation of electrons and holes^[15] and

iii) through directional design, COFs with light absorption, integrated oxidation and reduction centers can construct oxidation-reduction molecular junction that might simultaneously accomplish the WOR and ORR processes, and largely facilitate the charge transfer. To date, there are only rare COFs examples (e.g., COF-TfpBpy, TF_{50} -COF, COF-NUST-16, EBA-COF and CoPc-BTM-COF, etc)^[16] that have been applied in photosynthesis of H_2O_2 , and this field is still at the early stage with many unresolved issues to be addressed. Thus, it would be highly desirable to construct oxidation-reduction molecular junction COF based photocatalysts that can realize the full reaction photosynthesis of H_2O_2 to get rid of the usage of sacrificial agents, yet such powerful COF based photo-catalysts have been rarely synthesized and challenging in design to accomplish the integrated photo-synthesis to the best of our knowledge.

Here, for the first time, we have prepared a kind of oxidation-reduction molecular junction COF (denoted as TTF-BT-COF) with integrated oxidation and reduction centers, and can be successfully applied in the full reaction photosynthesis of H_2O_2 without sacrificial agents (Scheme 1). The covalent connection between the reducing group (BT) and oxidizing group (TTF) generates the oxidation-reduction junction that enables the visible light driven electron/holes to be effectively separated from the BT and transferred to the TTF part, resulting in photo excited electrons (BT, photo-reduction site) and holes (TTF, photo-oxidation site) that can be used for ORR and WOR, respectively. Specifically, its yield for H_2O_2 photosynthesis without sacrificial agents can be $\approx 276000 \mu\text{M h}^{-1} \text{g}^{-1}$, which is about 10 times higher than single linkers and physical mixture and represented to be the best H_2O_2 generation porous crystalline photocatalyst to date. Notably, it enables the facile generation of high concentration H_2O_2 ($\approx 18.7 \text{ wt} \%$) in long time batch-experiment that has much potential to be applied in practical applications. In addition, the oxidation-reduction molecular junction that can facilitate the charge-transfer and largely reduce the energy-barriers of both WOR and ORR to boost the performance has been verified by the theoretical calculations, which would extend



Scheme 1. Schematic representation of the oxidation-reduction molecular junction COF photocatalyst for full reaction photosynthesis of H_2O_2 .

the application potential of COFs in industrial scale H_2O_2 production.

Results and Discussion

TTF-BT-COF was synthesized by Schiff-base condensation between 2, 3, 6, 7-tetra (4-formylphenyl) tetrathiafulvalene (TTF-4CHO) and 4,4'-(benzo-2,1,3-thiadiazole-4,7-diyl)dianiline (BT-NH₂) by solvothermal method (Figure 1a). The crystalline structure of TTF-BT-COF was determined by the powder X-ray diffraction (PXRD) combined with theoretical structural simulations using Materials Studio version 7.0. An orthorhombic P222 space group based on TTF-BT-COF was built and performed Le Bail refinements of the PXRD patterns for full profile fitting against the proposed models, which provided a unit cell parameter of $a = 59.47 \text{ \AA}$, $b = 32.09 \text{ \AA}$, and $c = 4.26 \text{ \AA}$, $\alpha = \beta = \gamma = 90^\circ$ (Table S3). Moreover, the simulated PXRD pattern using AA stacking mode reproduced the experimentally observed curve while AB stacking did not, which was supported by the difference plot with unweighted-profile R factor (Rp) of 3.48% and weighted profile R factor (Rwp) of 4.44% (Figure 1b). In the PXRD pattern, it has intense peaks at 3.13° , 6.30° , 9.39° , and 12.53° , which can be assigned to the (1 1 0), (2 2 0), (3 3 0) and (4 4 0) facets of TTF-BT-COF, respectively. In addition, oriented lattice fringes can be observed in high-resolution TEM (HR-TEM) images and the lattice spacing of 1.41 nm is assigned to the (2 2 0) plane of TTF-BT-COF, confirming the high crystallinity of the obtained TTF-BT-COF (Figure 1d). Fourier transform infrared spectroscopy (FTIR) and ¹³C solid-state NMR spectroscopy (¹³C ssNMR) were used to confirm the chemical structure of TTF-BT-COF. In the FTIR spectra, the C=N stretching vibration and at 1620 cm^{-1} appears in the resultant TTF-BT-COF, while the C=O stretching vibration band at 1700 cm^{-1} and NH₂ vibration band at 3200--

3500 cm^{-1} belonged to reactant monomers that decreases obviously (Figure S2). Furthermore, the characteristic peak of ca. 158.9 ppm in ¹³C ssNMR corresponds to the carbon atom of the C=N bond (Figure S1). These results indicate that TTF-BT-COF has been successfully synthesized through the condensation reaction.^[3,17]

To investigate the chemical states of the existed elements in TTF-BT-COF, X-ray photoelectron spectroscopy (XPS) measurements have been conducted. For the XPS spectra of TTF-BT-COF, three main peaks with binding energy of 164.31, 284.60, 398.36 eV are ascribed to S 2p, C 1s, N 1s, respectively (Figure S3). In the C 1s region, the peaks appearing at 284.6 and 288.1 eV can be featured in C–O/C–N and C=C of TTF-BT-COF, respectively. In the S 2p region, two kinds of peaks with binding energies of 164.07 eV (S 2p_{3/2}) and 165.68 eV (S 2p_{1/2}) can be attributed to the characteristic peaks of sulfur (C–S) in TTF-4CHO unit and sulfur (N–S) in BT-NH₂. Besides, the N 1s spectra of TTF-BT-COF reveals a single peak at 398.36 eV, corresponding to the C=N/C–N of TTF-BT-COF.^[18] The fast Fourier transformation image of high-resolution transmission electron microscopy (HR-TEM) shows the hexagonal pore structure arrangement along the (1 0 0) crystal axis, which can also manifest the AA-stacking mode of the 2D TTF-BT-COF structure (Figure 1d). The morphology of TTF-BT-COF has also been characterized by scanning electron microscopy (SEM). The result shows that TTF-BT-COF is composed of solid spheres with a diameter of 400–600 nm. In addition, energy dispersive X-ray spectroscopy (EDS) analysis shows that C, N, S are uniformly distributed on TTF-BT-COF (Figure 1c). Similarly, TTF-pT-COF with benzothiadiazole (BT) monomer replaced by 4,4'-diamino-p-terphenyl (pT) and TPE-BT-COF (also called Etta-Td)^[19] with 2,3,6,7-tetra (4-formylphenyl)-tetrathiafulvalene (TTF-4CHO) monomer replaced by 4,4',4'',4'''-(ethene-1,1,2,2-tetrayl) tetrabenzaldehyde (TPE) were also prepared as the contrast samples for TTF-BT-COF (Table S4–5). Specifically, TTF-pT-COF as a kind of newly designed COF and its PXRD pattern shows high crystallinity that is in good agreement with the simulated structure (Figure S4). Moreover, the component and morphology of TTF-BT-COF have also been characterized by FT-IR, XPS and SEM tests (Figure S5–7).

Stability is a key factor to evaluate the durability of the catalysts in various applications. To investigate the chemical stability of TTF-BT-COF, TTF-pT-COF and TPE-BT-COF, the samples are soaking in diverse solutions for 5 days. For example, taking TTF-BT-COF for instance, the inherent structure of TTF-BT-COF remains intact after immersing in different solvents (i.e. N, N-dimethylformamide, acetonitrile, methanol and H₂O) for more than 5 days. After tests, the samples were characterized by the PXRD and FTIR tests. The PXRD results before and after the experiments show that the crystallinity of TTF-BT-COF immersed in different solutions remains intact, which is further proved by the similar FTIR spectrum (Figure S8–9).

Based on the ultraviolet and visible (UV/Vis) absorption spectra, TTF-BT-COF, TTF-pT-COF and TPE-BT-COF all have absorption in the visible light range (400–800 nm)

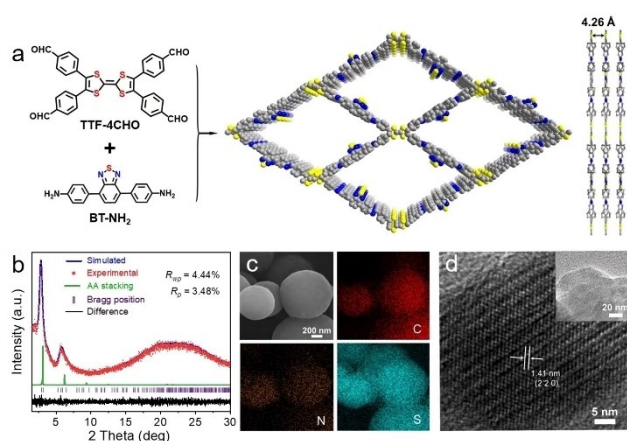


Figure 1. Structure and characterization of TTF-BT-COF. (a) Schematic representation of the synthesis of TTF-BT-COF. (b) Experimental (red dot) and simulated (blue line) PXRD patterns of TTF-BT-COF. (c) SEM and elemental mapping images of TTF-BT-COF. (d) HRTEM image and lattice fringes.

(Figure 2a). The band gaps (E_g) of TTF-BT-COF, TTF-pT-COF and TPE-BT-COF are determined to be 1.64, 1.71 and 2.16 eV by their Tauc plots, indicating that they have the characteristics of semiconductor (Figure 2b). The highest occupied molecular orbital (HOMO) of TTF-BT-COF, TTF-pT-COF and TPE-BT-COF were determined by ultraviolet photoelectron spectroscopy (UPS), from which the HOMO of TTF-BT-COF was estimated to be -6.69 eV (*vs.* vacuum level, E_v) by subtracting the excitation energy of 21.22 eV from the width of the He I UPS spectrum. Likewise, the HOMOs of TTF-pT-COF and TPE-BT-COF were determined to be -6.68 eV and -7.14 eV (*vs.* E_v), respectively (Figure S7–10). In order to verify the accuracy of these results, we further carried out the Mott Schottky electrochemical measurements to determine the energy band positions of TTF-BT-COF, TTF-pT-COF and TPE-BT-COF (Figure S13–15). Based on the results, the LUMO of TTF-BT-COF, TTF-pT-COF and TPE-BT-COF are calculated to be 0.21 V, 0.13 V, and 0.14 V (*vs.* NHE, pH 7), respectively. Meanwhile, the HOMO positions of TTF-BT-COF, TTF-pT-COF and TPE-BT-COF are 1.85 V, 1.84 V and 2.30 V (*vs.* NHE, pH 7), respectively, which are well associated with UV/Vis absorption spectra (Figure 2e).^[20] Notably, these results are also consistent with the values obtained by ultraviolet photoelectron spectroscopy (UPS) (Figure S10–12). Obviously, the band structures of TTF-BT-

COF, TTF-pT-COF and TPE-BT-COF are basically sufficient for the synthesis of H_2O_2 from both H_2O ($E_{H_2O_2/H_2O} = +1.76$ V *vs.* NHE) and O_2 ($E_{H_2O_2/O_2} = +0.68$ V *vs.* NHE) as shown in Figure 2e.^[21] Therefore, in theory, these COFs can be used as effective photocatalysts for full reaction photosynthesis of H_2O_2 owing to their suitable energy band structures. In addition, transient photocurrent response and photoluminescence (PL) measurements have been conducted to investigate the charge-transfer behaviors (Figure 2d). The transient-photocurrent-response intensity of TTF-BT-COF is much higher than those of TTF-pT-COF and TPE-BT-COF, as shown in Figure 2c. The PL of TTF-BT-COF is much lower than that of TTF-pT-COF and TPE-BT-COF (Figure 2d). These results show that the covalent bonding between TTF and BT can effectively enhance the electron hole separation and prevent the electron hole recombination, which might be attributed to the effective electron transfer caused by the covalent bonding between the oxidizing group and the reducing group. At the same time, in the measurement of electrochemical impedance spectroscopy (EIS), it is found that the electronic conductivity of TTF-BT-COF is also superior to that of TTF-pT-COF and TPE-BT-COF as proved by its smaller radius of the front semicircle (Figure 2f), indicating that the covalent connection between TTF and BT can significantly enhance the charge transfer.^[22] In order to further reveal the superiority of TTF-BT-COF, we also investigate the two redox ligands (*i.e.* TTF and BT). According to the ultraviolet and visible (UV/Vis) absorption spectra, both TTF and BT present absorption in the visible light range (400–800 nm) (Figure S16). The band gaps (E_g) of TTF and BT are determined to be 1.78 and 2.16 eV by their Tauc plots, indicating that they have the characteristics of semiconductor (Figure S16). In order to verify the accuracy of these results, we further carried out Mott Schottky electrochemical measurements to determine the energy band positions of TTF and BT (Figure S17). Based on these results, the LUMO of TTF and BT are calculated to be -0.02 V and 0.25 V (*vs.* NHE, pH 7), respectively. Meanwhile, the HOMO positions of TTF and BT locate at 1.76 V and 2.41 V (*vs.* NHE, pH 7), respectively, which are well associated with UV/Vis absorption spectra (Figure S18).

The experiment of visible light photosynthesis of H_2O_2 was carried out in pure O_2 atmosphere in aqueous solution without additional sacrificial agents and the yield of H_2O_2 was determined by iodometry and titanium sulfate colorimetry (Figure S22–25).^[23] A detailed description of the H_2O_2 photosynthesis experiment is introduced in the Supporting Information (detail see Methods). Figure 3a shows the photocatalytic performances of TTF-BT-COF, TTF-pT-COF and TPE-BT-COF and there exists significant linear relationship between H_2O_2 production and irradiation time. In the presence of TTF-BT-COF, the H_2O_2 concentration gradually increases with the increase of reaction time (0 to 60 min) and finally reaches to $1380 \mu M h^{-1}$, which is about 3 and 5 times higher than that of TTF-pT-COF ($498 \mu M h^{-1}$) and TPE-BT-COF ($296 \mu M h^{-1}$), respectively (Figure 3a). In addition, in order to prove the superiority of oxidation-reduction molecular junction in TTF-BT-COF,

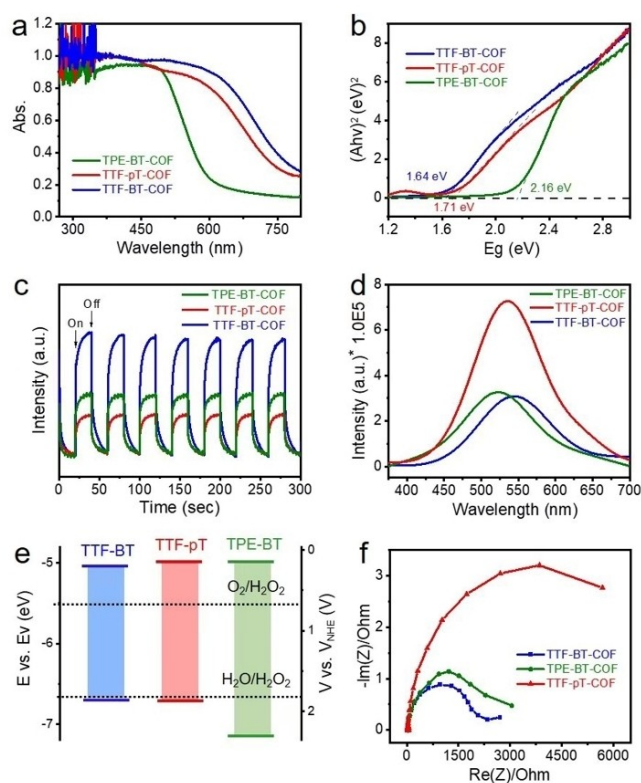


Figure 2. Characterizations of the optical properties for TTF-BT-COF, TTF-pT-COF and TPE-BT-COF. (a) UV/Vis absorption spectra. (b) Tauc plot for band gap calculation. (c) Transient photocurrent response. (d) The steady-state photoluminescence (PL) measurements. (e) Band-structure diagram. (f) Nyquist plots.

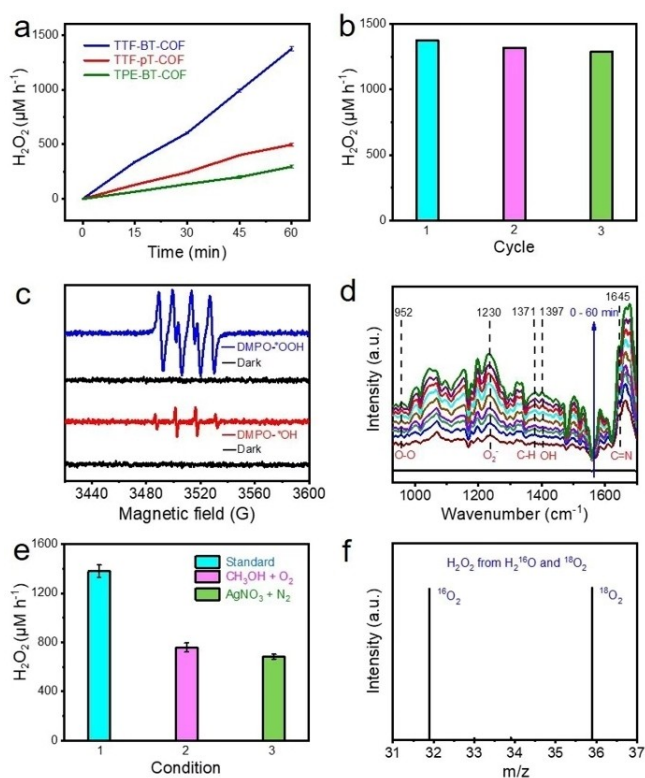


Figure 3. Performance of TTF-BT-COF, TTF-pT-COF and TPE-BT-COF photocatalyzed H₂O₂. (a) Photocatalytic activity of TTF-BT-COF, TTF-pT-COF and TPE-BT-COF for H₂O₂ production in pure water and O₂ atmosphere. (b) Cycling performance of TTF-BT-COF. (c) EPR signals of the reaction solution under the dark and visible light illumination in the presence of DMPO as the spin-trapping reagents. (d) DRIFTS spectrum of TTF-BT-COF in H₂O₂ photosynthesis. (e) Amounts of H₂O₂ produced on TTF-BT-COF in AgNO₃ (electron acceptor) solution and CH₃OH (hole acceptor) solvent. (f) ¹⁸O₂ isotope experiment to explore the source of H₂O₂.

we further evaluated the performances of TTF, BT and their physical mixture. Under visible light irradiation, the H₂O₂ production rates for TTF, BT and physical mixture are 98, 158 and 169 μMh⁻¹, respectively (Figure S26), which are much inferior to that of TTF-BT-COF. This result verifies that the establishment of oxidation-reduction molecular junction in TTF-BT-COF might accelerate both of the WOR and ORR processes to increase the efficiency for full reaction photosynthesis of H₂O₂. Noteworthy, under no sacrificial agent conditions, the yield of H₂O₂ of TTF-BT-COF can reach ≈276000 μMh⁻¹g⁻¹, which is the best H₂O₂ generation porous crystalline photocatalyst to date (Table S1–2). It is worth noting that it can easily generate high concentration H₂O₂ (≈18.7 wt %) in long time batch-experiment, which has great potential in practical application (Figure S27). Besides, the apparent quantum yield (AQY) between 420 nm is 11.19 % with a solar chemical conversion (SCC) efficiency of 0.49 %, which is higher than the typical photosynthetic efficiency of plants (0.10 %).^[24] Notably, the achieved SCC efficiency of TTF-BT-COF in full reaction photosynthesis of H₂O₂ is almost twice higher than that

without WOR (0.25 %), proving the superiority of the full reaction photosynthesis of H₂O₂.

Besides, the cycling stability is a vital factor to evaluate the durability of the photocatalyst. Thus, we have carried out the cycling tests. After three cycles of photocatalytic tests, the catalytic performance remains almost unchanged and the H₂O₂ yield can still be stable at 1300 μMh⁻¹, proving the high cycling stability of TTF-BT-COF (Figure 3b). Furthermore, the structural integrity of TTF-BT-COF is also confirmed by the PXRD tests (Figure S19). In the FTIR spectrum, TTF-BT-COF still exhibits C=N stretching vibration at 1620 cm⁻¹, while the C=O stretching vibration band at 1700 cm⁻¹ and NH₂ at 3200–3500 cm⁻¹ are similar to the state before reaction (Figure S20). At the same time, the XPS spectra before and after the photocatalytic reaction have been compared and the binding energies of the four main peaks of S 2p, C 1s, N 1s and O 1s remain unchanged (Figure S21). Above all, TTF-BT-COF exhibits high structural stability during the photocatalytic reaction.

In order to study the overall reaction of photocatalytic H₂O₂ production, the half reactions of TTF-BT-COF with saturated O₂ in methanol aqueous solution (methanol as electron donor) and the semi-redox reaction with N₂ in AgNO₃ aqueous solution (Ag⁺ as electron acceptor) were studied (Figure 3e).^[13a] Under the condition of O₂ atmosphere and deionized water (the standard condition), the H₂O₂ yield enhances linearly with the increase of irradiation time. In the half reactions with sacrificial agents (i.e. methanol and AgNO₃), the ORR reaction rate is almost the same as the WOR reaction rate, which also confirms that both WOR and ORR existed for TTF-BT-COF that can generate H₂O₂ through the 2e⁻ transfer process. In addition, ¹⁸O₂ isotope experiments have been carried out to verify the ORR and WOR processes (Figure 3f). TTF-BT-COF is irradiated in H₂¹⁶O and ¹⁸O₂ gas for 4 h. After removing unreacted gas with Ar gas, MnO₂ is added to the reaction system to decompose H₂O₂ and release O₂. The escaped gas is analyzed by gas chromatography-mass spectrometry. The decomposition products of photo-generated H₂O₂ through the MnO₂ reaction are close to 1:1 for ¹⁸O₂ and ¹⁶O₂, which shows that the utilization rate of atoms for H₂O and O₂ reaction to produce H₂O₂ is close to 100 %, and the H₂O₂ photosynthesis process experiences both the 2e⁻ ORR and 2e⁻ WOR pathways.

In order to study the mechanism of full reaction photosynthesis of H₂O₂ by TTF-BT-COF, 5,5-dimethylpyrroline N-oxide (DMPO) is applied as a free radical spin trapping agent to determine [•]OOH and [•]OH in electron paramagnetic resonance (EPR) (Figure 3c). The typical characteristic signals for DMPO-[•]OOH and DMPO-[•]OH are markedly observed in TTF-BT-COF under light irradiation (Figure 3c), which are absent under dark condition, indicating the generation of [•]OOH and [•]OH intermediate species. Based on the above analysis, we can draw a conclusion that the full reaction photosynthesis of H₂O₂ in this system is realized through the joint contribution of photogenerated electrons (e⁻), holes (h⁺), [•]OOH and [•]OH species.^[25] In addition, in order to study the mechanism of TPE-BT-COF and TTF-pT-COF on full reaction photosynthesis of H₂O₂,

DMPO is used as a free radical spin trapping agent to carry out EPR tests on them. Typical characteristic signals of $^*\text{OOH}$ and $^*\text{OH}$ can be clearly observed for TPE-BT-COF and TTF-pT-COF under light (Figure S28–29), which are also absent under dark condition. Based on the above experimental results, we speculate that their full reaction photosynthesis of H_2O_2 is completed by photogenerated electrons (e^-), holes (h^+), $^*\text{OOH}$ and $^*\text{OH}$ species. To further reveal the process of full reaction photosynthesis of H_2O_2 by TTF-BT-COF, we have performed the in situ diffuse reflectance infrared Fourier transform spectroscopy (DRIFTS) measurements to study the photocatalytic mechanism (Figure 3d). After the system is equilibrated, the vibrations corresponding to C–H (1371 cm^{-1}) and C=N (1645 cm^{-1}) for TTF-BT-COF are apparent. In addition, we also observe the obvious vibrations of the intermediates O–H (1397 cm^{-1}) and O–O (952 cm^{-1}) in the full reaction photosynthesis of H_2O_2 . This further proves that the catalytic mechanism of TTF-BT-COF photosynthesis of H_2O_2 is the synergistic effect of ORR and WOR (i.e. $^*\text{OOH}$ and $^*\text{OH}$) coupling with different intermediates produced at the same time.

We further study the $2e^-$ ORR and $2e^-$ WOR pathways of TTF-BT-COF, TPE-BT-COF and TTF-pT-COF measured by rotating disk electrode (RDE) and rotating ring disk electrode (RRDE).^[16a] As shown in Figure S30–32, we have calculated that the average electron transfer numbers of samples through RDE tests, during which the potential scanning range of rotating disc electrode is -1.0 – 0.2 V (vs Ag/AgCl), the scanning rate is 10 mVs^{-1} , and the potential of platinum ring electrode is 0.23 V . Specifically, the average electron transfer numbers of TTF-BT-COF, TPE-BT-COF and TTF-pT-COF at -0.8 V (vs Ag/AgCl) in the ORR reactions are 2.31, 2.27 and 2.43, respectively, implying they are all $2e^-$ transferring ORR processes. To reveal the $2e^-$ WOR process, the RRDE tests have been conducted under N_2 condition (Figure S33–35), during which the potential scanning range of the rotating disc electrode is 1.2 – 2.6 V (vs Ag/AgCl), the scanning rate is 10 mVs^{-1} , and the constant potential of the platinum ring electrode is -0.23 V (vs Ag/AgCl).^[16a,26] In general, the $1e^-$ product with highly active nature can be hardly generated under this applied potential (1.2 – 2.6 V). In this setting, if O_2 is generated in $4e^-$ WOR by rotating the disk electrode, it can be swept to the ring electrode and reduced with relative detection signal, thus creating an ideal testing condition to reveal the potential electron transfer number of the system. As shown in Figure S33, the increasing disk currents with potentials higher than 1.7 V (solid lines, vs Ag/AgCl) indicate that WOR occurs at the rotating disk electrode for TTF-BT-COF. Specifically, no reduction current is observed for TTF-BT-COF at the Pt ring electrode, suggesting that TTF-BT-COF cannot generate O_2 via $4e^-$ WOR process. Specifically, the reduction current has not been observed for TTF-BT-COF on the Pt ring electrode, indicating that TTF-BT-COF cannot generate O_2 through WOR ($4e^-$ WOR process). However, when the potential applied on the ring electrode changes to $+0.6\text{ V}$ (vs Ag/AgCl), a higher oxidation current can be detected for TTF-BT-COF due to the oxidation of

H_2O_2 occurs on the Pt ring electrode (Figure S33). Similarly, TPE-BT-COF and TTF-pT-COF present similar phenomena. Hence, the RDE and RRDE measurements support that H_2O_2 photosynthesis underwent $2e^-$ ORR and $2e^-$ WOR pathways for these three COFs (Figure S34–35).

Based on the above experiments and analysis, a possible mechanism is proposed to illustrate the photosynthesis of H_2O_2 by TTF-BT-COF (Figure 4a): driven by visible-light irradiation, the photoinduced electron transfer process takes place from TTF (HOMO) to BT (LUMO) after absorbing photons. Then O_2 gets the electron to generate active intermediate ($^*\text{OOH}$), while H_2O uses the holes to form $^*\text{OH}$ at the same time. After that, $^*\text{OH}$ and $^*\text{OOH}$ simultaneously produce H_2O_2 at relative oxidation and reduction sites on TTF-BT-COF, respectively, thus achieving the superior performance in H_2O_2 generation. Firstly, the charge distribution of TTF-BT-COF structure is analyzed by differential charge density. The interfacial charge density difference is depicted in Figure 4b, in which the charge accumulation is shown as the yellow region of thiazole on BT, and the charge depletion is shown as the

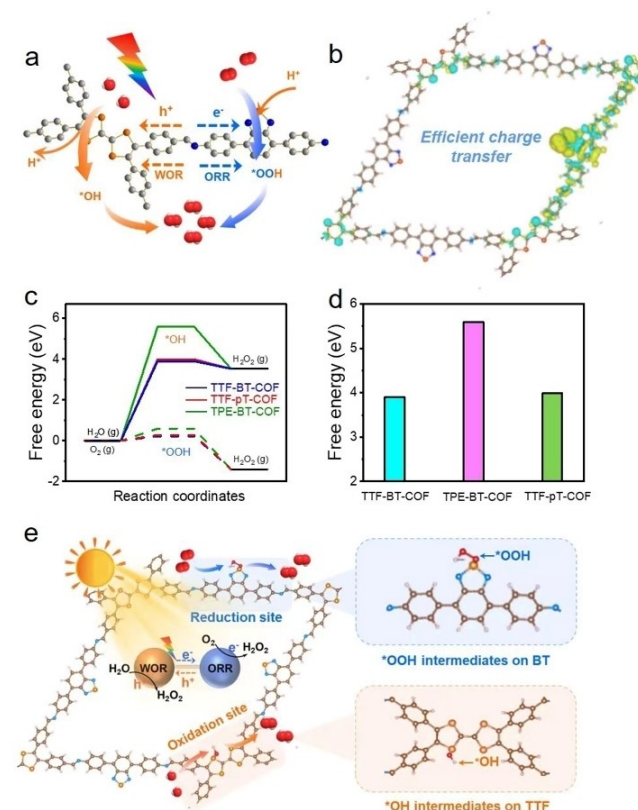


Figure 4. DFT calculations and the proposed reaction mechanism. (a) Schematic diagram of the photosynthesis of H_2O_2 through the ORR and WOR pathways. (b) Differential charge density diagram of TTF-BT-COF. (c) Free energy diagram of the TTF-BT-COF, TTF-pT-COF and TPE-BT-COF for photosynthesis of H_2O_2 through the WOR (full line) and ORR (break line) pathways. (d) Free energy change histogram of TTF-BT-COF, TTF-pT-COF and TPE-BT-COF for H_2O_2 production by $^*\text{OH}$ intermediates. (e) Adsorption configuration of $^*\text{OH}$ intermediates on TTF and $^*\text{OOH}$ intermediates on BT of the TTF-BT-COF.

blue region close to S atoms on TTF. The differential charge density diagram shows that the S atom at the BT site has better electronegativity, and the oxygen adsorbed on the BT site is easier to get electrons to generate ORR, while the S atom in TTF has relatively weak electronegativity, and the water molecules adsorbed on the TTF site use holes to generate WOR. Therefore, TTF-BT-COF has the possible active sites that can simultaneously complete ORR and WOR to generate H₂O₂.

Based on this, we have calculated the free energy changes of *OH and *OOH adsorbed by TTF-BT-COF, TTF-pT-COF and TPE-BT-COF during the production of H₂O₂ by ORR and WOR, respectively (Figure 4c). There are two pathways for photosynthesizing H₂O₂ (i.e. WOR and ORR) with different intermediates. Photocatalytic WOR to generate H₂O₂ requires two steps: from H₂O to *OH and then two *OH further combine to form H₂O₂, in which the first process is the rate determination step (RDS) (Figure 4d). As shown in Figure 4e, the sites where TTF-BT-COF and TTF-pT-COF adsorb *OH are S sites of TTF. Under the interaction of TTF-BT-COF, the energy barrier of intermediate *OH produced by adsorption of WOR at S site is 3.90 eV, while the energy barrier of TTF-pT-COF is 3.99 eV, respectively, proving the synergistic role of BT linker in reducing the energy barrier of the whole structure than pT linker. For TPE-BT-COF, the energy barrier of *OH adsorption at the N site of C=N bond is as high as 5.59 eV, indicating the superior role of TTF in WOR (Figure S36). These results indicate that TTF-BT-COF is more favorable for the WOR to generate H₂O₂ more than TTF-pT-COF and TPE-BT-COF. For the photocatalytic ORR process, it contains two steps: from O₂ to *OOH and then the *OOH combines with the hydrogen proton to generate H₂O₂ (Figure 4a). The first process is the RDS. As shown in Figure S36 and Figure 4e, TTF-BT-COF and TPE-BT-COF adsorb *OOH at the S sites on BT (Figure 4e). Compared with the high-energy barrier of TPE-BT-COF (0.59 eV), TTF-BT-COF is only 0.22 eV, which indicates that the synergistic role of TTF linker in reducing the energy barrier of the whole structure than TPE linker. For TTF-pT-COF, the energy barrier of *OOH adsorption at the N site of C=N bond is as high as 0.28 eV, indicating the superior role of BT in ORR (Figure 4e, S37).

According to the above theoretical calculation results, it can be concluded that TTF-BT-COF is more favorable to adsorb *OH and *OOH intermediates generated by WOR and ORR than TTF-pT-COF and TPE-BT-COF. To be specific, under visible light irradiation, the photogenerated electrons and holes separated and transferred to the BT and TTF, respectively. Then, ORR and WOR occur simultaneously on these two ligands (Figure 4c). On TTF, the conversion of H₂O to H₂O₂ requires two steps: from H₂O dehydrogenates to *OH and then two *OH further combine to form H₂O₂, in which the first process is the rate determination step (RDS) with the energy barrier of 3.90 eV. Accordingly, for the photocatalytic ORR process, it contains two hydrogenation steps: from O₂ to *OOH and then the *OOH combines with the hydrogen proton to generate H₂O₂ (Figure 4c). The first process is the RDS with

the energy barrier of 0.22 eV. Among them, hydrogen protons removed by WOR are used for the ORR, thus ensuring the charge balance of the catalytic system. According to the above-mentioned experiment and calculation results, as shown in Figure 4a and 4e, a favorable photosynthesis of H₂O₂ mechanism, namely, the formation of oxidation-reduction molecular junction in TTF-BT-COF, has been proposed that can accelerate the separation of electrons and holes, which makes it easier for O₂ and H₂O to capture electrons and use the holes to form active intermediates, respectively, finally forming H₂O₂.

Conclusion

In summary, we have prepared a kind of oxidation-reduction molecular junction COF (TTF-BT-COF) through the covalent-coupling of tetrathiafulvalene (photo-oxidation site) and benzothiazole (photo-reduction site) and can be successfully applied in the full reaction photosynthesis of H₂O₂ without sacrificial agents. The covalent connection between them generates the oxidation-reduction junction and presents visible-light-adsorption region, effective electron-hole separation-efficiency and suitable photo-redox ability that enables the visible light driven electrons to be effectively transferred from BT to TTF, thus resulting in the simultaneously accomplished ORR and WOR reactions. It is worth noting that its production rate ($\approx 276000 \mu\text{M h}^{-1} \text{g}^{-1}$) for H₂O₂ photosynthesis without sacrificial agents can be record-high among porous crystalline photocatalysts, which is about 10 times higher than single linkers or physical mixture. In addition, it enables the facile generation of high concentration H₂O₂ ($\approx 18.7 \text{ wt} \%$) in long-time batch experiment, holding much potential in practical applications. Furthermore, the oxidation-reduction molecular junction that can facilitate the charge-transfer and largely reduce the energy-barriers of both WOR and ORR to boost the performance have been proved by theoretical calculations. This is the first work that can design oxidation-reduction molecular junction COF for full reaction photosynthesis of H₂O₂, which might shed fresh light on the exploration of porous crystalline materials in potentially industrial scale H₂O₂ production.

Supplemental Information includes 37 figures, 5 tables.

Acknowledgements

This work was financially supported by the NSFC (Grants 21871141, 21871142, 21901122, 22071109, 22105080, 22171139).

Conflict of Interest

The authors declare no conflict of interest.

Data Availability Statement

The data that support the findings of this study are available from the corresponding author upon reasonable request.

Keywords: Covalent Organic Framework · Full Reaction · H₂O₂ · Oxidation-Reduction Molecular Junction · Photocatalysis

- [1] a) Y.-X. Ye, J. Pan, F. Xie, L. Gong, S. Huang, Z. Ke, F. Zhu, J. Xu, G. Ouyang, *Proc. Natl. Acad. Sci. USA* **2021**, *118*, e2103964118; b) Y. Sun, L. Han, P. Strasser, *Chem. Soc. Rev.* **2020**, *49*, 6605–6631; c) R. J. Lewis, K. Ueura, X. Liu, Y. Fukuta, T. E. Davies, D. J. Morgan, L. Chen, J. Qi, J. Singleton, J. K. Edwards, S. J. Freakley, C. J. Kiely, Y. Yamamoto, G. J. Hutchings, *Science* **2022**, *376*, 615–620; d) J. Chen, Q. Ma, X. Zheng, Y. Fang, J. Wang, S. Dong, *Nat. Commun.* **2022**, *13*, 2808.
- [2] D. Guo, R. Shibuya, C. Akiba, S. Saji, T. Kondo, J. Nakamura, *Science* **2016**, *351*, 361–365.
- [3] Y. Shiraishi, M. Matsumoto, S. Ichikawa, S. Tanaka, T. Hirai, *J. Am. Chem. Soc.* **2021**, *143*, 12590–12599.
- [4] S. Zaman, L. Huang, A. I. Douka, H. Yang, B. You, B. Y. Xia, *Angew. Chem. Int. Ed.* **2021**, *60*, 17832–17852; *Angew. Chem.* **2021**, *133*, 17976–17996.
- [5] a) G. M. Lari, B. Puértolas, M. Shahrokhi, N. López, J. Pérez-Ramírez, *Angew. Chem. Int. Ed.* **2017**, *56*, 1775–1779; *Angew. Chem.* **2017**, *129*, 1801–1805; b) Y. Gu, S. Wu, Y. Cao, M. Liu, S. Chen, X. Quan, H. Yu, *ACS Appl. Mater. Interfaces* **2021**, *13*, 56045–56053.
- [6] H. Hou, X. Zeng, X. Zhang, *Angew. Chem. Int. Ed.* **2020**, *59*, 17356–17376; *Angew. Chem.* **2020**, *132*, 17508–17529.
- [7] a) J. M. Campos-Martin, G. Blanco-Brieva, J. L. G. Fierro, *Angew. Chem. Int. Ed.* **2006**, *45*, 6962–6984; *Angew. Chem.* **2006**, *118*, 7116–7139; b) A. Huang, R. S. Delima, Y. Kim, E. W. Lees, F. G. L. Parlange, D. J. Dvorak, M. B. Rooney, R. P. Jansonius, A. G. Fink, Z. Zhang, C. P. Berlinguette, *J. Am. Chem. Soc.* **2022**, *144*, 14548–14554.
- [8] a) Y. Shiraishi, T. Takii, T. Hagi, S. Mori, Y. Kofuji, Y. Kitagawa, S. Tanaka, S. Ichikawa, T. Hirai, *Nat. Mater.* **2019**, *18*, 985–993; b) Z. Zhang, T. Tsuchimochi, T. Ina, Y. Kumabe, S. Muto, K. Ohara, H. Yamada, S. L. Ten-no, T. Tachikawa, *Nat. Commun.* **2022**, *13*, 1499; c) C. Dong, Y. Yang, X. Hu, Y. Cho, G. Jang, Y. Ao, L. Wang, J. Shen, J. H. Park, K. Zhang, *Nat. Commun.* **2022**, *13*, 4982; d) R. Mehrotra, D. Oh, J.-W. Jang, *Nat. Commun.* **2021**, *12*, 6644; e) H. He, X. Wu, H. Xian, J. Zhu, Y. Yang, Y. Lv, Y. Li, K. O. Konhauser, *Nat. Commun.* **2021**, *12*, 6611.
- [9] a) J. H. Baek, T. M. Gill, H. Abroshan, S. Park, X. Shi, J. Nørskov, H. S. Jung, S. Siahrostami, X. Zheng, *ACS Energy Lett.* **2019**, *4*, 720–728; b) J. Xu, X. Zheng, Z. Feng, Z. Lu, Z. Zhang, W. Huang, Y. Li, D. Vuckovic, Y. Li, S. Dai, G. Chen, K. Wang, H. Wang, J. K. Chen, W. Mitch, Y. Cui, *Nat. Sustainability* **2021**, *4*, 233–241.
- [10] T. Liu, Z. Pan, J. J. M. Vequizo, K. Kato, B. Wu, A. Yamakata, K. Katayama, B. Chen, C. Chu, K. Domen, *Nat. Commun.* **2022**, *13*, 1034.
- [11] J. Ma, X. Peng, Z. Zhou, H. Yang, K. Wu, Z. Fang, D. Han, Y. Fang, S. Liu, Y. Shen, Y. Zhang, *Angew. Chem. Int. Ed.* **2022**, *61*, e202210856; *Angew. Chem.* **2022**, *134*, e202210856.
- [12] a) G.-h. Moon, W. Kim, A. D. Bokare, N.-e. Sung, W. Choi, *Energy Environ. Sci.* **2014**, *7*, 4023–4028; b) C. Chu, D. Huang, Q. Zhu, E. Stavitski, J. A. Spies, Z. Pan, J. Mao, H. L. Xin, C. A. Schmuttenmaer, S. Hu, J.-H. Kim, *ACS Catal.* **2019**, *9*, 626–631; c) X. Zeng, Y. Liu, Y. Kang, Q. Li, Y. Xia, Y. Zhu, H. Hou, M. H. Uddin, T. R. Gengenbach, D. Xia, C. Sun, D. T. McCarthy, A. Deletic, J. Yu, X. Zhang, *ACS Catal.* **2020**, *10*, 3697–3706.
- [13] a) Z. Teng, Q. Zhang, H. Yang, K. Kato, W. Yang, Y.-R. Lu, S. Liu, C. Wang, A. Yamakata, C. Su, B. Liu, T. Ohno, *Nat. Catal.* **2021**, *4*, 374–384; b) L. Liu, M.-Y. Gao, H. Yang, X. Wang, X. Li, A. I. Cooper, *J. Am. Chem. Soc.* **2021**, *143*, 19287–19293.
- [14] a) S. Kandambeth, K. Dey, R. Banerjee, *J. Am. Chem. Soc.* **2019**, *141*, 1807–1822; b) D. Jiang, *Chem* **2020**, *6*, 2461–2483; c) A. P. Côté, A. I. Benin, N. W. Ockwig, M. O’Keeffe, A. J. Matzger, O. M. Yaghi, *Science* **2005**, *310*, 1166–1170; d) J. Yuan, X. You, N. A. Khan, R. Li, R. Zhang, J. Shen, L. Cao, M. Long, Y. Liu, Z. Xu, H. Wu, Z. Jiang, *Nat. Commun.* **2022**, *13*, 3826; e) W. Zhao, P. Yan, B. Li, M. Bahri, L. Liu, X. Zhou, R. Clowes, N. D. Browning, Y. Wu, J. W. Ward, A. I. Cooper, *J. Am. Chem. Soc.* **2022**, *144*, 9902–9909; f) S. Chai, X. Chen, X. Zhang, Y. Fang, R. S. Sprick, X. Chen, *Environ. Sci. Nano* **2022**, *9*, 2464–2469.
- [15] a) Y. Li, L. Yang, H. He, L. Sun, H. Wang, X. Fang, Y. Zhao, D. Zheng, Y. Qi, Z. Li, W. Deng, *Nat. Commun.* **2022**, *13*, 1355; b) Z. Xiong, B. Sun, H. Zou, R. Wang, Q. Fang, Z. Zhang, S. Qiu, *J. Am. Chem. Soc.* **2022**, *144*, 6583–6593; c) C. Krishnaraj, H. Sekhar Jena, L. Bourda, A. Laemont, P. Pachfule, J. Roeser, C. V. Chandran, S. Borgmans, S. M. J. Rogge, K. Leus, C. V. Stevens, J. A. Martens, V. Van Speybroeck, E. Breynaert, A. Thomas, P. Van Der Voort, *J. Am. Chem. Soc.* **2020**, *142*, 20107–20116; d) Y.-X. Li, W. Choi, *Chem Catal.* **2022**, *2*, 1517–1519.
- [16] a) M. Kou, Y. Wang, Y. Xu, L. Ye, Y. Huang, B. Jia, H. Li, J. Ren, Y. Deng, J. Chen, Y. Zhou, K. Lei, L. Wang, W. Liu, H. Huang, T. Ma, *Angew. Chem. Int. Ed.* **2022**, *61*, e202200413; *Angew. Chem.* **2022**, *134*, e202200413; b) H. Wang, C. Yang, F. Chen, G. Zheng, Q. Han, *Angew. Chem. Int. Ed.* **2022**, *61*, e202202328; *Angew. Chem.* **2022**, *134*, e202202328; c) Q. Zhi, W. Liu, R. Jiang, X. Zhan, Y. Jin, X. Chen, X. Yang, K. Wang, W. Cao, D. Qi, D. Jiang, *J. Am. Chem. Soc.* **2022**, *144*, 21328–21336; d) F. Tan, Y. Zheng, Z. Zhou, H. Wang, X. Dong, J. Yang, Z. Ou, H. Qi, W. Liu, Z. Zheng, X. Chen, *CCS Chem.* **2022**, *4*, 3751–3761; e) M. Wu, Z. Shan, J. Wang, T. Liu, G. Zhang, *Chem. Eng. J.* **2023**, *454*, 140121; f) L. Zhai, Z. Xie, C.-X. Cui, X. Yang, Q. Xu, X. Ke, M. Liu, L.-B. Qu, X. Chen, L. Mi, *Chem. Mater.* **2022**, *34*, 5232–5240.
- [17] a) X. Ding, L. Chen, Y. Honsho, X. Feng, O. Saengsawang, J. Guo, A. Saeki, S. Seki, S. Irle, S. Nagase, V. Parasuk, D. Jiang, *J. Am. Chem. Soc.* **2011**, *133*, 14510–14513; b) M. Wang, P. Zhang, X. Liang, J. Zhao, Y. Liu, Y. Cao, H. Wang, Y. Chen, Z. Zhang, F. Pan, Z. Zhang, Z. Jiang, *Nat. Sustainability* **2022**, *5*, 518–526.
- [18] M. Lu, J. Liu, Q. Li, M. Zhang, M. Liu, J.-L. Wang, D.-Q. Yuan, Y.-Q. Lan, *Angew. Chem. Int. Ed.* **2019**, *58*, 12392–12397; *Angew. Chem.* **2019**, *131*, 12522–12527.
- [19] S. Wang, Q. Sun, W. Chen, Y. Tang, B. Aguila, Y. Pan, A. Zheng, Z. Yang, L. Wojtas, S. Ma, F.-S. Xiao, *Matter* **2020**, *2*, 416–427.
- [20] a) J.-N. Chang, Q. Li, Y. Yan, J.-W. Shi, J. Zhou, M. Lu, M. Zhang, H.-M. Ding, Y. Chen, S.-L. Li, Y.-Q. Lan, *Angew. Chem. Int. Ed.* **2022**, *61*, e202209289; *Angew. Chem.* **2022**, *134*, e202209289; b) J. Liu, Y. Liu, N. Liu, Y. Han, X. Zhang, H. Huang, Y. Lifshitz, S.-T. Lee, J. Zhong, Z. Kang, *Science* **2015**, *347*, 970–974.
- [21] a) Y. Kofuji, Y. Isobe, Y. Shiraishi, H. Sakamoto, S. Tanaka, S. Ichikawa, T. Hirai, *J. Am. Chem. Soc.* **2016**, *138*, 10019–10025; b) J. García-Serna, T. Moreno, P. Biasi, M. J. Cocero, J.-P. Mikkola, T. O. Salmi, *Green Chem.* **2014**, *16*, 2320–2343.
- [22] Y.-R. Wang, H.-M. Ding, X.-Y. Ma, M. Liu, Y.-L. Yang, Y. Chen, S.-L. Li, Y.-Q. Lan, *Angew. Chem. Int. Ed.* **2022**, *61*, e202114648; *Angew. Chem.* **2022**, *134*, e202114648.

- [23] Z. Wei, M. Liu, Z. Zhang, W. Yao, H. Tan, Y. Zhu, *Energy Environ. Sci.* **2018**, *11*, 2581–2589.
- [24] a) W. Zhao, P. Yan, B. Li, M. Bahri, L. Liu, X. Zhou, R. Clowes, N. D. Browning, Y. Wu, J. W. Ward, A. I. Cooper, *J. Am. Chem. Soc.* **2022**, *144*, 9902–9909; b) L. Chen, L. Wang, Y. Wan, Y. Zhang, Z. Qi, X. Wu, H. Xu, *Adv. Mater.* **2020**, *32*, 1904433.
- [25] a) Y. Isaka, Y. Kawase, Y. Kuwahara, K. Mori, H. Yamashita, *Angew. Chem. Int. Ed.* **2019**, *58*, 5402–5406; *Angew. Chem.* **2019**, *131*, 5456–5460; b) H.-Y. Jiang, P. Zhou, Y. Wang, R. Duan, C. Chen, W. Song, J. Zhao, *Adv. Mater.* **2016**, *28*, 9776–9781.
- [26] X. Shi, S. Siahrostami, G.-L. Li, Y. Zhang, P. Chakthranont, F. Studt, T. F. Jaramillo, X. Zheng, J. K. Nørskov, *Nat. Commun.* **2017**, *8*, 701.

Manuscript received: December 21, 2022

Accepted manuscript online: December 29, 2022

Version of record online: ■■, ■■

Research Articles

Photocatalytic H₂O₂ Synthesis

J.-N. Chang, Q. Li, J.-W. Shi, M. Zhang,
L. Zhang, S. Li, Y. Chen,* S.-L. Li, Y.-
Q. Lan* e202218868

Oxidation-Reduction Molecular Junction
Covalent Organic Frameworks for Full Re-
action Photosynthesis of H₂O₂



A kind of oxidation-reduction molecular junction covalent-organic-framework (TTF-BT-COF) has been prepared through the covalent-coupling between oxidation group (TTF) and reduction group (BT), which can be successfully applied for the efficient full reaction photosynthesis of H₂O₂.